LAWRENCE
LIVERMORE
NATIONAL
LABORATORY

LLNL-TR-673841

Inline CBET Model Including SRS Backscatter

D. S. Bailey

June 26, 2015

Disclaimer

This work performed under the auspices of the U.S. Department of Energy by Lawrence Livermore National Laboratory under Contract DE-AC52-07NA27344.

Inline CBET model including SRS backscatter

David Bailey

Lawrence Livermore National Laboratory, Livermore, CA 94551

Cross-beam energy transfer (CBET) has been used as a tool on the National Ignition Facility (NIF) since the first energetics experiments in 2009 to control the energy deposition in ignition hohlraums and tune the implosion symmetry. As large amounts of power are transferred between laser beams at the entrance holes of NIF hohlraums, the presence of many overlapping beat waves can lead to stochastic ion heating in the regions where laser beams overlap [P. Michel et al., Phys. Rev. Lett. **109**, 195004 (2012)]. Using the CBET gains derived in this paper, we show how to implement these equations in a ray-based laser source for a rad-hydro code.

I. INTRODUCTION

Overlapping multiple high power laser beams in plasmas can lead to cross-beam energy transfer (CBET), a process similar to Brillouin scattering in which the beat wave created by crossing laser beams drives a plasma oscillation that acts like a Bragg cell, scattering a beam in the direction of the other one [1, 2]. CBET has turned out to be a major player in inertial confinement fusion (ICF) experiments over the past few years, for both direct-drive and indirect-drive geometries. For indirect-drive experiments on the National Ignition Facility (NIF), control of CBET by wavelength separation tuning [3, 4] has been demonstrated at the beginning of the National Ignition Campaign in 2009 [5–7]. It has since then continuously been used as a tool to control the equatorial energy balance inside the "hohlraum" targets, and has even been developed further by adding additional wavelength tuning capabilities to control the polar symmetry or help mitigate backscatter by transferring laser energy away from the high-backscatter risk regions of the hohlraum and into the safer ones [8, 9]. On the other hand, for direct-drive experiments at the Omega facility, CBET moves energy from incoming laser beams into the refracted outer edges of outgoing laser beams, thus reducing the amount of laser energy being deposited into the coronal plasma [10–12].

In CBET, the amount of power being transferred depends on the amplitude of the density modulation driven by the ponderomotive force of the beat wave, and on the proximity of the driven oscillation to an ion acoustic mode of the plasma. For two laser beams with frequencies ω_m, ω_n and wave vectors $\boldsymbol{k}_m$, $\boldsymbol{k}_n$ driving a beat wave with wave vector $\boldsymbol{k} = \boldsymbol{k}_m - \boldsymbol{k}_n$ and frequency $\omega_k = \omega_m - \omega_n$, the coupling is thus maximum when the phase velocity of the beat wave in the frame of the plasma, $v_k = (\omega_k - \boldsymbol{k} \cdot \boldsymbol{V})/k$ (where $\boldsymbol{V}$ is the plasma flow), is equal to the plasma sound speed c_s, which will drive a plasma oscillation $\delta n_e/n_e$ (where n_e is the electron density) matching the ion acoustic wave dispersion relation (cf. Fig. 1). This is equivalent to a Bragg cell, with a modulation of the refractive index $N = \sqrt{1 - n_e/n_c}$ (where n_c is the critical density for the laser wavelength) traveling at the sound speed of the medium. On NIF, CBET is controlled by using different wavelengths for different cones of laser beams, i.e. v_k is adjusted via ω_k; typically, the corresponding wavelength shift $\Delta\lambda_k$ (with $\omega_k/\omega_0 = \Delta\lambda_k/\lambda_0$, where ω_0 and λ_0 are the laser frequency and wavelength) is a few Å, with $v_k < c_s$. Whereas on Omega, where all the beams have identical wavelength (ω_k=0) [13], CBET occurs because beams cross at the Mach 1 surface of the expanding coronal

plasma where $\boldsymbol{k} \cdot \boldsymbol{V} = kc_s$ (i.e. $v_k = c_s$ in the plasma frame).

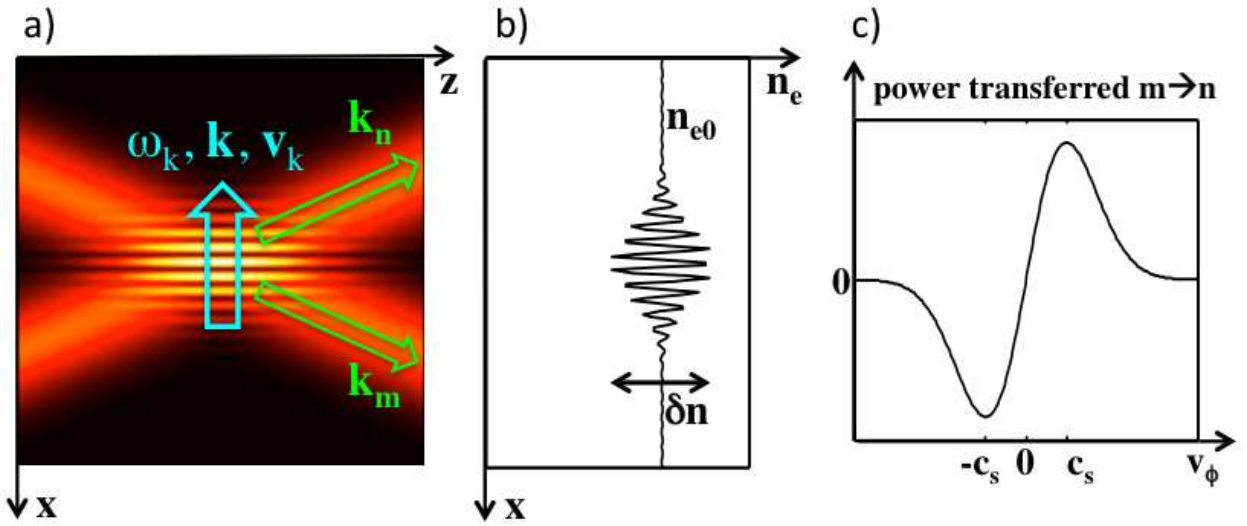

FIG. 1. Basic mechanism for CBET: a) two crossing laser beams with frequencies ω_m, ω_n and wave vectors $\boldsymbol{k}_m$, $\boldsymbol{k}_n$ drive a beat wave with frequency $\omega_k = \omega_m - \omega_n$, wave vector $\boldsymbol{k} = \boldsymbol{k}_m - \boldsymbol{k}_n$, and phase velocity $v_k = (\omega_k - \boldsymbol{k} \cdot \boldsymbol{V})/k$ in the frame of the plasma ($\boldsymbol{V}$ is the plasma flow velocity); b) the ponderomotive force from the beat wave drives a density modulation in the plasma, and hence a refractive index modulation, traveling at v_k; c) if $|v_k| = c_s$, the refractive index modulation acts as a Bragg cell scattering one laser beam in the direction of the other (i.e. energy transfer); being able to control v_k, e.g. via the frequency shift ω_k between the beams, allows to set the direction of power transfer (via the sign) and its amplitude (via the proximity of v_k to c_s).

CBET on NIF was initially predicted to be observable and controllable because of the small amplitudes of the density modulations created by the beat waves, preventing non-linear effects from occurring but still being large enough to allow significant amounts of transfer due to cumulative effects from multiple crossing, taking place in fairly uniform plasmas over very long ($\sim$ mm) distances [3, 5, 14, 15]. The ion acoustic waves are typically strongly damped, leading to broad resonance regions (as schematically represented in Fig. 1c) and amplification gains being less sensitive to gradients or non-uniformities in the plasma.

Calculations using the linear response of an ion wave to the beat ponderomotive force were in decent agreement with the 2009 experiments where NIF was typically delivering 200 TW of peak laser power with small wavelength separations ($\Delta\lambda$=1.5 - 5 Å) leading to small amounts of transfer. However, in more recent experiments, where peak laser power is

usually between 400 and 500 TW and where large amounts of power transfer are required to achieve symmetric implosions of the DT fuel capsule ($\Delta\lambda$=6 to 9 Å), linear calculations fail to reproduce the experimental observables, and in fact usually predict a full pump depletion of the NIF "outer beams" which has never been seen in experiments. An artificial limiter on the amplitude of the density modulations $\delta n/n$ driven by the beat waves has thus been introduced in the design calculations in order to recover some level of predictive capability [8, 11, 16]; it is however purely empirical and lacking physics justification, and the values at which one needs to saturate the waves are too low to be physically justified ($\delta n/n \simeq 10^{-4}$).

The initial design calculations incorporating the effects of CBET on NIF targets were done using an iterative sequence of simulations without any CBET coupled with off-line transfer calculations to adjust the beam powers for the next time interval. Aside from being tedious and labor intensive, these results were not self consistent. Hence there was a desire to include a self-consistent inline model into the major simulation codes. We present here a realization of such a model into an ICF simulation code.

II. MODEL EQUATIONS

A. Laser beam propagation

Let us first present the model equations and then discuss their implementation. For a laser beam α, the evolution of the intensity I_α along the beam path (which direction is noted z) is given by[4, 5, 17]:

$$\partial_z I_\alpha = \omega_\alpha \, \gamma_{\alpha\beta} \, I_\alpha I_\beta + \omega_\alpha \, \gamma_{\alpha R} \, I_\alpha I_R - \nu_\alpha \, I_\alpha. \tag{1}$$

The three terms on the RHS represent respectively: i) the CBET coupling to other beams β intersecting α in a given cell; ii) the SRS coupling; iii) the IB absorption.

The coupling term for SRS has in fact the same expression as for CBET: the coupling between our test beam α and β, whether β is another laser beam (CBET) or the companion SRS ray of α, is:

$$\gamma_{\alpha\beta} = \frac{\pi \, r_e}{2 \, m_e c^2} \, \frac{k_{\alpha\beta}^2}{k_\alpha k_\beta \, \omega_\alpha \omega_\beta} \, \Im[K_{\alpha\beta}] \, (1 + \cos^2 \theta_{\alpha\beta}), [18] \tag{2}$$

where r_e is the classical electron radius and m_e its mass, $k_{\alpha\beta} = |\boldsymbol{k}_\beta - \boldsymbol{k}_\alpha|$, $\boldsymbol{k}_\alpha$ is the wave vector of α; its norm is $k_\alpha = (2\pi/\lambda_\alpha)\sqrt{1 - n_e/n_{c\alpha}}$, $n_{c\alpha}$ is the critical electron density at the wavelength λ_α and $\theta_{\alpha\beta}$ is the angle between the propagation directions of beams α and β

$$\cos\theta_{\alpha\beta} = \frac{|\boldsymbol{k}_\alpha \cdot \boldsymbol{k}_\beta|}{|\boldsymbol{k}_\alpha||\boldsymbol{k}_\beta|}.$$

All the wavelengths, including the SRS wavelength, are given (this package is designed for "post-shot" simulations, where λ_R and $I_R(z_0)$, the SRS wavelength and backscatter intensity measured at the lens, are given at each time step, typically from SRS experimental measurements).

The coupling coefficient $K_{\alpha\beta}$ is given by:

$$K_{\alpha\beta} = \frac{\chi_{e,\alpha\beta}\,(1 + \chi_{i,\alpha\beta})}{1 + \chi_{e,\alpha\beta} + \chi_{i,\alpha\beta}}, \tag{3}$$

where the electron and ion susceptibilities are taken at the beat wave of α and β:

$$\chi_{e,\alpha\beta} = \frac{-1}{2(k_{\alpha\beta}\,\lambda_{De})^2}\,Z'\left[\frac{\omega_\beta - \omega_\alpha - (\boldsymbol{k}_\beta - \boldsymbol{k}_\alpha)\cdot\boldsymbol{V}}{\sqrt{2}\,k_{\alpha\beta}\,v_{Te}}\right] \tag{4}$$

$$\chi_{i,\alpha\beta} = \sum_{ions}\frac{-1}{2(k_{\alpha\beta}\,\lambda_{Di})^2}\,Z'\left[\frac{\omega_\beta - \omega_\alpha - (\boldsymbol{k}_\beta - \boldsymbol{k}_\alpha)\cdot\boldsymbol{V}}{\sqrt{2}\,k_{\alpha\,\beta}v_{Ti}}\right] \tag{5}$$

where ω_{pe} is the electron plasma frequency, λ_{De} is the electron Debye length (with $v_{Te} = \lambda_{De}\omega_{pe}$, where $v_{Te} = \sqrt{T_e/m_e}$ is the electron thermal velocity) and where

$$Z'[x] = -2\,(1 + x\,e^{-x^2}(\imath\sqrt{\pi} - 2\int_0^x dt\,e^{t^2})$$

is the derivative of the plasma dispersion function of real argument.

Similar definitions apply to the ions, but due the resonant nature of the coupling, it's important to explicitly perform the species sum.

Note that we have these symmetries for $Z'[x]$:

$$\Re\big[Z'[x]\big] = +\Re\big[Z'[-x]\big] \tag{6}$$

$$\Im\big[Z'[x]\big] = -\Im\big[Z'[-x]\big] \tag{7}$$

For the case of SRS, some simplifications arise:

- since $\theta_{\alpha R} = \pi$ (pure backscatter is assumed), $1 + \cos^2\theta_{\alpha R} = 2$ and $k_{\alpha R} = k_\alpha + k_R$;

- for typical SRS wavelengths, $\chi_{i\alpha R} \ll 1$ so $K_{\alpha R} \simeq \chi_{e,\alpha R}/(1+\chi_{e,\alpha R})$;
- the wavelength shift between the SRS light and the laser light is always much greater than the Döppler shift from the flow, so the $(\boldsymbol{k}_\beta - \boldsymbol{k}_\alpha)\cdot\boldsymbol{V}$ term in the argument of the Z' function can be ignored.

The SRS coupling coefficient thus simplifies to:

$$\gamma_{\alpha R} = \frac{\pi r_e}{m_e c^2}\,\frac{(k_\alpha + k_R)^2}{k_\alpha k_R\,\omega_\alpha \omega_R}\,\Im\left[\frac{\chi_{e,\alpha R}}{1+\chi_{e,\alpha R}}\right], \tag{8}$$

$$\chi_{e,\alpha R} = \frac{-1}{2(k_{\alpha R}\,\lambda_{De})^2}\,Z'\left[\frac{\omega_R - \omega_\alpha}{\sqrt{2}k_{\alpha R}\,v_{Te}}\right] \tag{9}$$

III. LASER RAY CBET IMPLEMENTATION

We use the 3D laser ray package [19] that performs the tracking calculation for an arbitrary number of laser beams with a user specified frequency and time dependent power for each laser. As shown in (1), the ray propagation equation depends on the intensities of all other beams that traverse the current cell containing this ray. To compute these intensities, during the initial tracking pass, the contribution of each ray is added to every cell the ray crosses: $\mathcal{I}_r = \overline{P}\,\tau_r/\Delta V$, where $\tau_r = (\int c\,ds/v_g)_r = (\int ds/\eta)_r$ is the cell crossing time, ΔV is the cell volume and $\overline{P}$ is the time-averaged power

$$\overline{P} = \frac{1}{\tau}\int_0^\tau d\tau'\,P(\tau') \tag{10}$$

which includes the effect of laser absorption by inverse-bremsstrahlung. The cell averaged $\bar{\nu}_{ib}$ is computed by an integral of the point coefficient using interpolated temperature and density values inside the cell for better accuracy. Hence (10) is evaluated as

$$\overline{P} = P(0)\,\frac{1 - exp(-\bar{\nu}_{ib}\,\tau)}{\bar{\nu}_{ib}\,\tau} \tag{11}$$

so that the individual ray contribution per cell becomes

$$\mathcal{I}_r = \overline{P}\,\tau_r/\Delta V = P(0)\,\frac{1 - exp(-\bar{\nu}_{ib}\,\tau)}{\bar{\nu}_{ib}\,\Delta V} \tag{12}$$

The total intensity for a given beam is just the ray sums

$$\mathcal{I} = \sum_r \mathcal{I}_r \tag{13}$$

Note that this intensity is the *swelled* intensity, unlike those in (1), so the beam coupling coefficients given below are corrected for this. Also, during the initial tracking pass, the local cell value of the k vector for each beam is accumulated as a power weighted sum of all the rays in that beam traversing the cell. This method thereby accounts for the effects of refraction and absorption on the beam's propagation in the plasma.

We rewrite the CBET propagation equation (1) for two coupled beams:

$$\partial_{\tau_1} \mathcal{I}_1 = p_{12}\, \alpha_2\, \eta_1\, C_{12}\, \mathcal{I}_2\, \mathcal{I}_1 \tag{14}$$

$$\partial_{\tau_2} \mathcal{I}_2 = p_{21}\, \alpha_1\, \eta_2\, C_{21}\, \mathcal{I}_1\, \mathcal{I}_2 \tag{15}$$

where $p_{12} = p_{21} = (1 + cos^2\theta_{12})/4$,

$$\alpha_{1,2}^{-1} = \frac{\epsilon_0}{2}\, (\frac{m_e c^2}{e})^2\, k_{1,2}^v\, \omega_{1,2}$$

is the natural unit of intensity for a laser with frequency $\omega_{1,2}$, [20]
$\eta_{1,2} = v_{g_{1,2}}/c = \sqrt{1 - n_e/n_{c_{1,2}}}$, and

$$C_{12} = \frac{k_{12}^2}{4\, k_1}\, \Im[K_{12}]$$

where K_{12} is defined by (3).
We can now write the ray propagation equations (14), (15) in terms of the cell intensities:

$$\partial_{\tau_1} \sum_{r_1} \overline{P}_{r_1}\, \tau_{r_1}|_2 = p_{12}\, \alpha_2\, \eta_1\, C_{12}\, \mathcal{I}_2\, (\sum_{r_1} \overline{P}_{r_1}\, \tau_{r_1}) \tag{16}$$

$$\partial_{\tau_2} \sum_{r_2} \overline{P}_{r_2}\, \tau_{r_2}|_1 = p_{12}\, \alpha_1\, \eta_2\, C_{21}\, \mathcal{I}_1\, (\sum_{r_2} \overline{P}_{r_2}\, \tau_{r_2}) \tag{17}$$

To obtain the total beam transfer powers, we iteratively compute the pairwise coupling for all active beams. Generalization of equations (16,17) to more than two beams and summing rays for the total intensity of a single beam in a cell leads to

$$\partial_{\tau_1} \sum_{r_1} \overline{P}_{r_1} \tau_{r_1} = \sum_q \left(p_{1q}\, \alpha_q\, \eta_1\, C_{1q}\, \mathcal{I}_q \sum_{r_1} \overline{P}_{r_1} \tau_{r_1} \right) / \Delta V, \tag{18}$$

where the sum over q includes all beams with non-zero intensities in the cell traversed by the rays r_1.

Integrating (16,17) for two individual coupled rays in a cell we get the power transfer relations

$$\delta\, \overline{P}_{r_1}|_2 = p_{12}\, \alpha_2\, \eta_1\, C_{12}\, \mathcal{I}_2\, (\overline{P}_{r_1}\, \tau_1) \tag{19}$$

$$\delta\, \overline{P}_{r_2}|_1 = p_{12}\, \alpha_1\, \eta_2\, C_{21}\, \mathcal{I}_1\, (\overline{P}_{r_2}\, \tau_2) \tag{20}$$

Using the symmetries of Z' from (6,(7)) and summing over all rays in a cell we obtain the relation for two beams

$$\frac{\sum_{r_1} \delta\, \overline{P}_{r_1}|_2}{\sum_{r_2} \delta\, \overline{P}_{r_2}|_1} = \frac{\alpha_2\, \eta_1\, C_{12}}{\alpha_1\, \eta_2\, C_{21}} = -\frac{\alpha_2\, \eta_1\, k_2}{\alpha_1\, \eta_2\, k_1} = -\frac{\lambda_2^v}{\lambda_1^v} = -\frac{\omega_1}{\omega_2} \tag{21}$$

or

$$\Delta P_{12} \lambda_1^v = -\Delta P_{21} \lambda_2^v \tag{22}$$

and from energy conservation we obtain the ion acoustic power

$$\Delta P^{ia} = \Delta P_{12} + \Delta P_{21} = \Delta P_{12} \left(1 - \frac{\omega_2 - (\boldsymbol{k}_2 - \boldsymbol{k}_1) \cdot \boldsymbol{V}}{\omega_1} \right) \tag{23}$$

The Döppler shift term is included to account for the ion acoustic wave deposition that occurs even for zero wavelength shift for non-colinear beams. [21]
It is convenient to symmetrize (23) as:

$$\delta \overline{P}^{ia}_{r_1}|_2 = \frac{1}{2}\, \delta \overline{P}_{r_1}|_2 \left(1 - \frac{\omega_2 - (\boldsymbol{k}_2 - \boldsymbol{k}_1) \cdot \boldsymbol{V}}{\omega_1} \right) \tag{24}$$

$$\delta \overline{P}^{ia}_{r_2}|_1 = \frac{1}{2} \delta\, \overline{P}_{r_2}|_1 \left(1 - \frac{\omega_1 - (\boldsymbol{k}_1 - \boldsymbol{k}_2) \cdot \boldsymbol{V}}{\omega_2} \right) \tag{25}$$

A. Intensity iteration algorithm

A self-consistent solution to (18) requires iteratively adjusting the cell intensities to account for the cross beam coupling given by (16,17) for each ray, which is accumulated over all rays to get the updated cell intensities. The total power transfer between beams $(b_q, b_{q'})$ is given by the sum:

$$\Delta\overline{P}_{qq'} = \sum_{cells_{qq'}} \sum_{r_q} \delta\overline{P}_{r_q}|_{q'} \tag{26}$$

In (26) the sum over cells includes those that are simultaneously traversed by rays from b_q and $b_{q'}$.

Using energy conservation, the iteration converges when

$$\sum_{q<q'} \Big(\Delta\overline{P}_{qq'} + \Delta\overline{P}_{q'q} \Big) = \sum_{q<q'} \Big(\Delta\overline{P}^{ia}_{qq'} + \Delta\overline{P}^{ia}_{q'q} \Big) \tag{27}$$

to some user-specified tolerance:

$$error < tol \; \frac{|LHS - RHS|_{(27)}}{\sum_{q<q'} \Big(\Delta\overline{P}_{qq'} > 0 + \Delta\overline{P}_{q'q} > 0 \Big)} \tag{28}$$

To accelerate the intensity iteration, we save the final intensity results from the previous time step and use those intensities to initiate the solution of (1) for each ray. Employing this scheme, we have observed typical iteration counts less than three on current ICF target simulations. Finally, we re-compute the laser pondermotive force to account for the beam power shifts due to the CBET couplings, using the same algorithm which calculates the non-transfer forces [22]. This algorithm includes both scalar and tensor components of the forces which is possible because of the 3D tracking method.

B. Saturation model

From the fundamental coupling equation (1) we can see that at high laser intensities, the coupling can increase without bound. In real life, stochastic ion heating saturates the CBET

mechanism by increasing the ion acoustic velocity beyond the phase velocity of the externally driven beat waves, driving them off-resonance. For a spatially under-resolved simulation, the heating is spread over such a large volume that there is insufficient moderation of the CBET coupling rate, leading to errors in the calculation. To address this, as discussed in [17], we therefore apply an upper bound to the plasma wave amplitude to limit $|\delta n_e/n_e| < 10^{-3}$. The density perturbation is driven by the pondermotive force due to the driven beat waves and can be written:

$$\left|\frac{\delta n_e}{n_e}\right|_{qq'} = \left(\frac{k_{qq'}^2\, c^2}{2\,\omega_{pe}^2}\right) |K_{qq'}| \,\sqrt{p_{qq'}\,\alpha_q \mathcal{I}_q\,\alpha_{q'}\mathcal{I}_{q'}} \tag{29}$$

where $K_{qq'}$ is given by (3), and we note the expression is clearly symmetric in q, q'. Hence to enforce the amplitude limit, we re-write the $C_{qq'}$ of (14) as:

$$C_{qq'} \longrightarrow \min\left[\left|\frac{\delta n_e}{n_e}\right|_{qq'}, S_t\right] \left(\frac{\omega_{pe}^2}{2\,k_q\,c^2}\right) \frac{\Im[K_{qq'}]}{|K_{qq'}|} \,/\sqrt{p_{qq'}\,\alpha_q \mathcal{I}_q\,\alpha'_q \mathcal{I}_{q'}} \tag{30}$$

where the user set saturation limit S_t is normally taken as 10^{-3}. The saturation calculation by default is only computed once before the intensity iteration loop, which in tests has shown not to significantly affect the final results.

IV. CBET EXAMPLE PROBLEM

To test the in-line CBET algorithm, we have run several comparisons to the off-line code of Pierre Michel. One of the more complete examples is presented here. This example used a uniform plasma cylinder with a prescribed velocity to test both terms in the arguments of Z' in equations (4,5).

- Laser parameters:
  - 24 NIF quads from upper hemisphere (same θ's, ϕ's and spot sizes as NIF), focused at $x = y = z = 0$ (propagating towards $z < 0$)
  - $\Delta\lambda = -4.5\,\text{Å}\,(@\,1\,\omega)$ on inner cones, with 1 TW power on all quads
- Plasma conditions:

  - CH (50/50 atomic fraction, $C_1\,H_1$ composition); $T_e = 1\,keV, T_i = 0.7\,keV$
    $n_e = 2\%\ n_c\ (1.8 \cdot 10^{20}\,cm^{-3}\ @\,3\,\omega)$
  - uniform flow along $z > 0 : V_z = +\,c/1000$; no saturation limit used

- Numerical controls:

  - rays/beam: 5000 in Hydra and Lasnex, 650-1300 in script
    (number of pixels/beam varies with beam size and box resolution)
  - simulation box: $100 \times 100 \times 100$ cylinder in Hydra and Lasnex,
    $300 \times 300 \times 300$ in script (Cartesian, $\delta z = 30\,\mu m, \delta x = \delta y = 40\,\mu m$)

In Fig. 2 we show the spatial profiles of the laser beams after the interaction region. Note that the resulting intensities are much different from the initial equal intensities, and that the 30° beams have large intensity variations across the spots, they are 'hollowed out'. The effect of increased resolution can also be observed in the smoothness of the script results compared to the Hydra ones. It is rarely possible to use sufficient resolution in a real NIF design calculation that would match the script's, but tests have shown that the transfer powers are rather insensitive to both the number of rays and the spatial resolution.

In Fig. 3 we show a comparison of the final beam powers relative to the initial ones, with dramatic changes from the equal initial powers. These results also show excellent agreement between the script and the inline calculations.

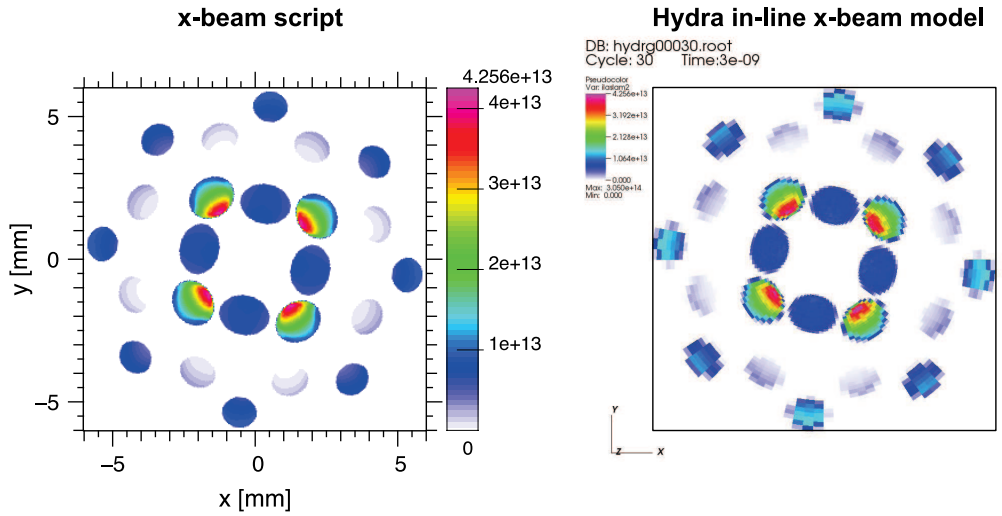

FIG. 2. Laser beams intensity profiles at $z = -4.5\,mm$ post-transfer with all quads well separated.

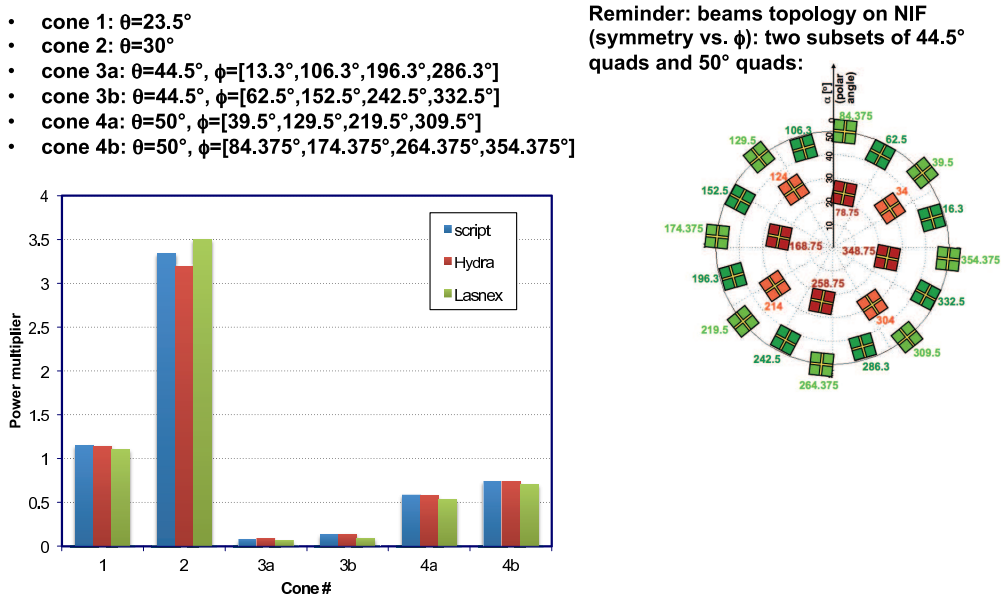

FIG. 3. Beam powers for NIF cones after CBET transfer. All the calculations agree very well, and show that the coupling moved power from the outer cones to the inner ones. The Döppler term for this example was chosen to be comparable in magnitude to the wavelength shift term.

V. COMPANION SRS RAY

This package assumes that an SRS ray propagates along each laser ray, following the same path from the lens to the interior of the target. In reality, SRS propagates in the opposite

direction as the laser, but we can easily calculate the propagation backwards, starting from the lens and simply inverting the signs of the various terms.

The propagation equation for the companion SRS ray, noted R, along the same path as the laser ray α, is therefore similar to (1):

$$\partial_z I_R = \omega_R \gamma_{\alpha R} I_\alpha I_R + \nu_R I_R. \tag{31}$$

Because the SRS propagation is calculated backwards, the exponential growth due to the coupling to the laser pump (first RHS term) is negative (i.e. it has the same sign as the second term on the RHS of (1); $\gamma_{\alpha\beta}$ is negative for $\lambda_\beta > \lambda_\alpha$, which is always the case if β represents the SRS ray). Likewise, the IB absorption (second RHS term) becomes positive (i.e. exponential growth). The SRS propagation will therefore have to be interrupted as soon as the IB absorption becomes larger than the SRS amplification gain. This is the "convective gain threshold", i.e. the threshold for existence of the SRS light (cf. examples and preliminary tests in the next section).

The coupling of the SRS ray to other laser (or SRS) rays, also known as "re-amplification", is neglected (experiments by J.D. Moody et al. on NIF have demonstrated that the effect is at most very small). This can be re-assessed in the future if needed.

A. Method

The SRS is assumed to exactly follow its companion laser ray. Its intensity needs to be tracked in order to adjust the coupling between the laser and the SRS, however there is no need to "launch" new SRS rays (one just needs to keep track of an extra quantity, $I_R(z)$, along each laser ray).

The IB energy deposited in the plasma also needs to account both the laser and the SRS absorption (calculated from Eqs. (1) and (31)). We use the Manley-Rowe relations to accumulate the Langmuir wave energy so that it's possible to inject that energy as a source of hot electrons.

Finally, one must not forget to terminate the SRS coupling as soon as the threshold for convective gain has been reached, i.e. as soon as:

$$\nu_R \geq -\omega_R \gamma_{\alpha R} I_\alpha \tag{32}$$

However, in general it's possible for the SRS intensity to vary in a non-monotonic fashion, so to check for this, a global pre-scan is made to find the true minimum intensity along the complete ray trajectory. This minimum point is then set as the origin of the SRS ray.

The contributions of the SRS rays to the laser pondermotive force is included together with that of the main pump beams.

VI. EXAMPLE FOR ONE RAY ALONG A TYPICAL NIF-ICF HYDRO PROFILE (SRS ONLY, NO CBET)

We illustrate the scheme by calculating the coupled laser and SRS intensities from Eqs. (1, 31) in the absence of CBET (i.e. setting the first RHS term of (1) to zero).

We simply trace a straight ray following the centroid of a 30° NIF quad in the hydrodynamics profiles calculated by a Lasnex simulation [23], as shown in Fig. 4. The green line is the ray, propagating at 30° from Z=6.5 ("z_0") to Z=1 mm ("z_f"), where Z is the hohlraum axis; the color axis represents n_e/n_c.

The electron density and temperature along the ray, as well as the SRS gain, are shown in Fig. 5. We first show the total gain integrated along the ray as a function of λ_1, the SRS wavelength; this gain is calculated for a fixed pump (laser) intensity of 10^{15} W/cm^2 in vacuum. It is thus equal to $-\omega_1 I_0 \int dz\, \gamma_{01}(z)$ (cf. (31); we changed the sign in order to show the positive SRS gain exponent along $-z$), where the integral is taken along the ray.

This is then used to get the wavelength of maximum gain, which in this case is 577 nm (close to the experimental measurement). Fixing λ_1 to this wavelength, we then calculate the gain rate along the ray (bottom-right plot), i.e. $-\omega_1 I_0 \gamma_{01}(z)$. The gain rate peaks near Z=1.6 mm; in other words, the "real-life" expectation is that SRS will trigger from the region near Z=1.6 mm at a wavelength near λ_1=577 nm.

Figure 6 shows the result of applying the coupled-mode equations (Eqs. (1) and (31)) along the test-ray for λ_1=577 nm, and using as input conditions $I_0(z_0) = 10^{15}$ W/cm^2 and $I_1(z_0) = 3.5 \cdot 10^{14}$ W/cm^2 (i.e. assuming 35% measured SRS reflectivity; the boundary z_0 corresponds to Z=6.5 mm).

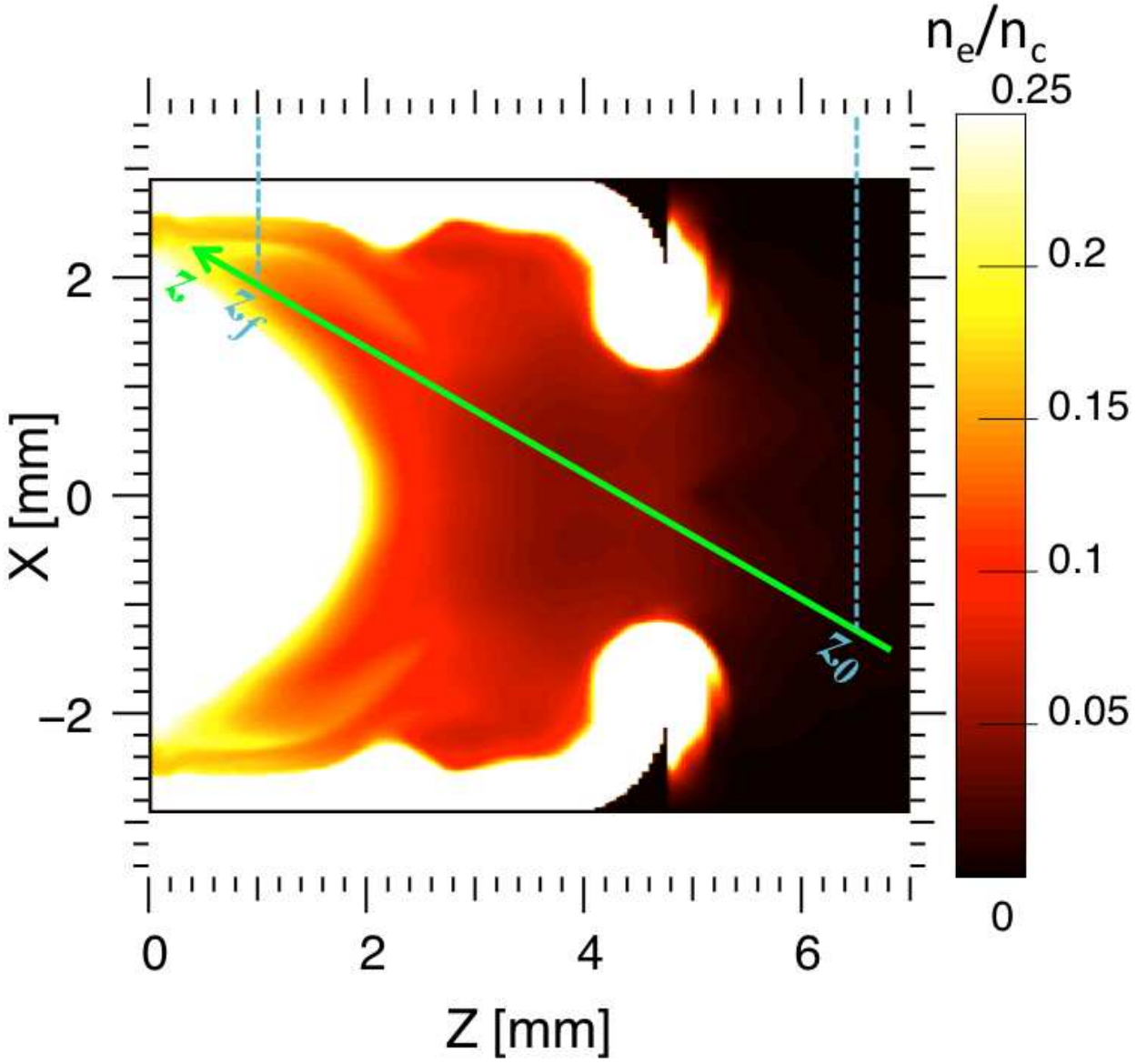

FIG. 4. Hydrodynamics simulation used for this test (from Lasnex post-shot N110807); the model will be tested on the green ray propagating straight (no refraction) along the centroid of a 30° NIF quad from Z=6.5 to Z=1 mm.

As expected, the laser decays as it propagates towards the interior of the hohlraum, due to both its IB absorption in the plasma and its depletion to the SRS ray. The SRS intensity calculation, done backwards, also shows its depletion due to coupling to the laser until it reaches the point convective gain threshold, near z=1.35 mm (zoomed-in insert in Fig. 6), where Eq. (32) is no longer satisfied. At this point, SRS has reached its "inner" boundary

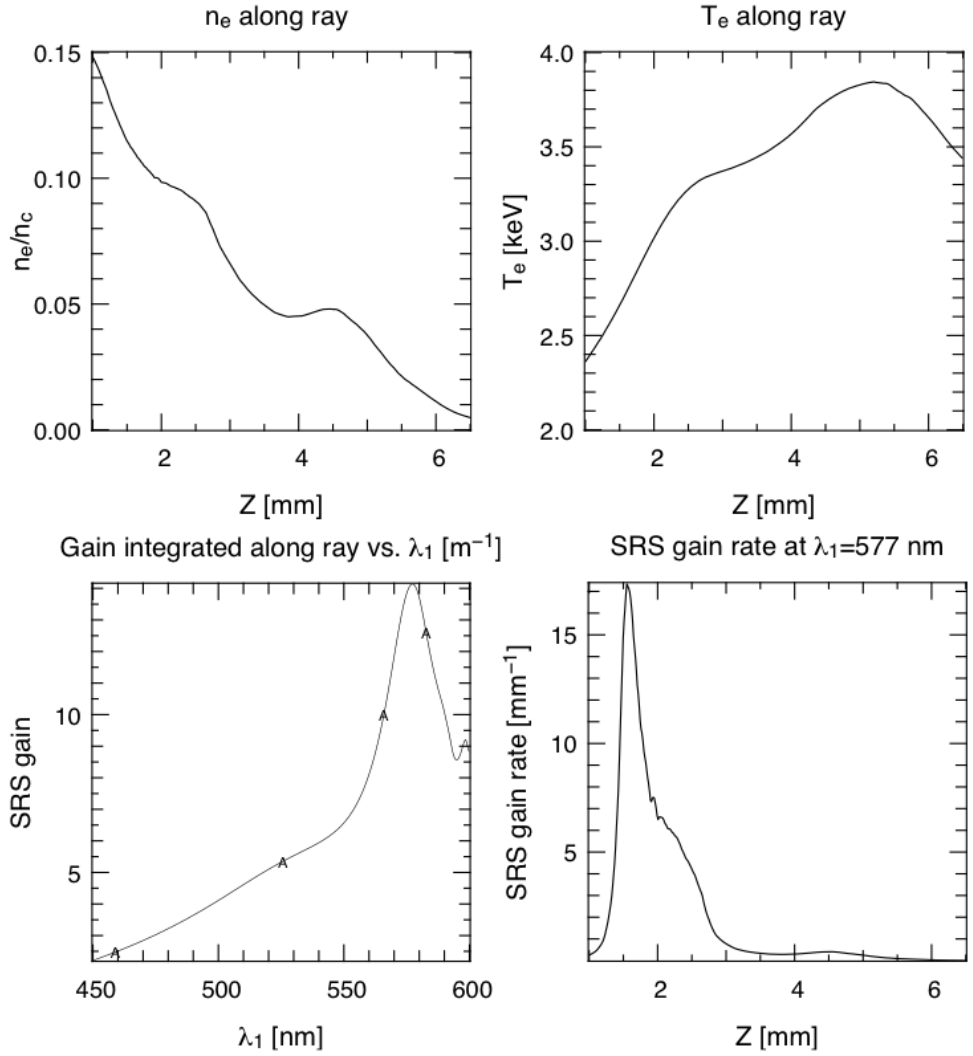

FIG. 5. Hydrodynamics quantities along the test-ray: electron density and temperature, SRS gain (integrated along the ray) vs. SRS wavelength λ_1, and SRS gain rate (in mm$^-$1) along the ray for the SRS wavelength of maximum gain (λ_1=577 nm). On these figures, Z is the position along the ray projected on the hohlraum axis (from Z=1 to 6.5 mm).

value of $\sim 7 \cdot 10^{12}$ W/cm^2, and must then be turned off.

Following the "real" SRS propagation direction along $-z$, this means that SRS starts at Z=1.35 mm with an intensity of $7 \cdot 10^{12}$ W/cm^2, and grows exponentially (while also being re-absorbed, but the exponential growth overcomes the re-absorption) until it reaches its final measured value of $3.5 \cdot 10^{14}$ W/cm^2 at Z=6.5 mm.

This also means that the SRS only got amplified by a factor 50. In reality, SRS is

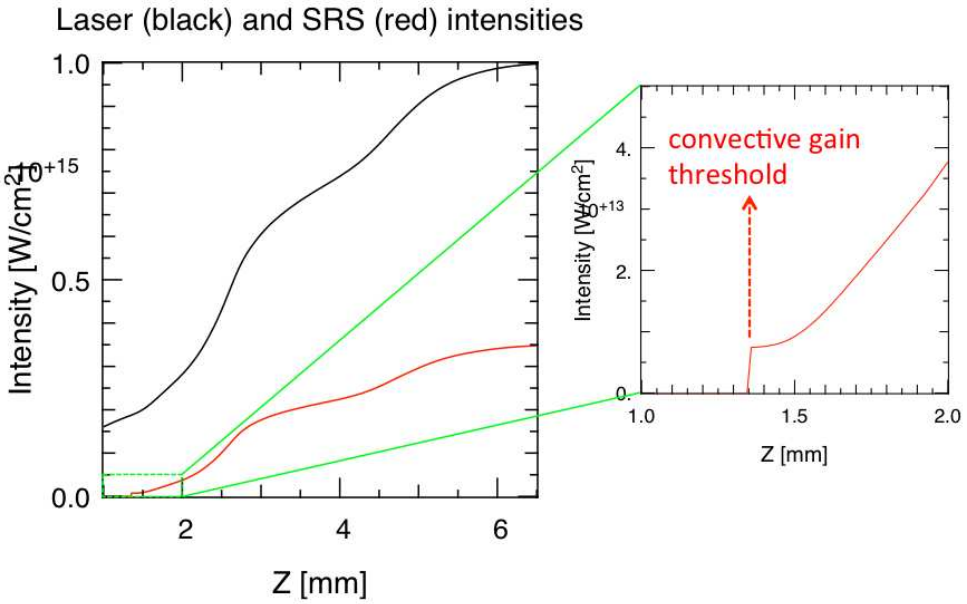

FIG. 6. Michel's solution of the laser and SRS coupled mode equations (Eqs. (1) and (31)) along the test-ray. The insert is a zoomed-in plot of the SRS intensity as it reaches the point of convective gain threshold along the ray, i.e. when Eq. (32) is no longer satisfied. At this point, the SRS intensity must be forced to zero (SRS can not exist anymore beyond this point, since any growth would be beaten by re-absorption).

expected to start from noise levels and be amplified by about 10^8-10^9. However most of the amplification is expected to occur over a very short distance (few speckles lengths): our scheme will obviously miss this part, which would be too difficult to evaluate anyway since it is due to complicated non-linear phenomena (effects of laser speckles, kinetic effects etc.). But the remaining amplification out of the resonance region is what will matter most from an energetics (i.e. hydrodynamics) point of view, and is what we are trying to model here.

In Figure 7 a comparison of Michel's script calculation to an inline calculation is shown. The excellent agreement gives confidence that the inline calculation can provide an accurate self-consistent model for design simulations.

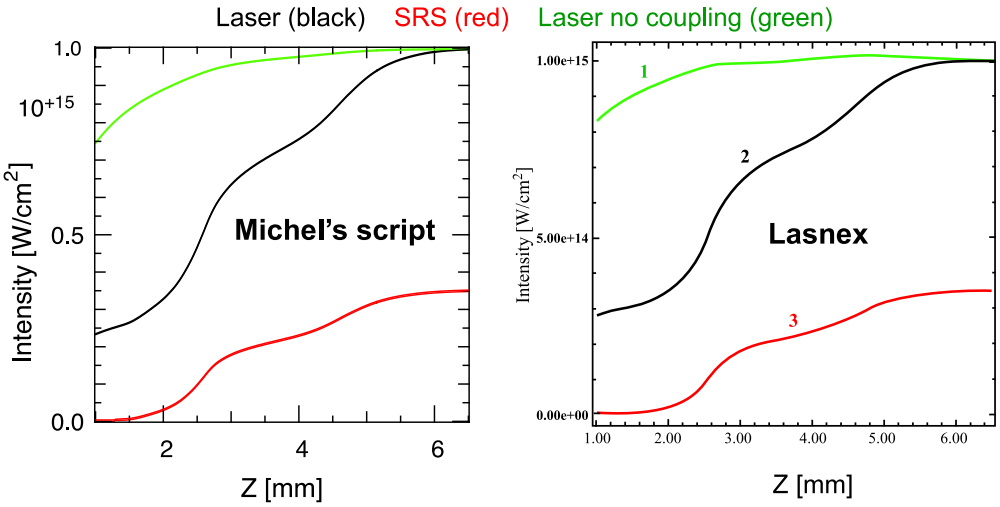

FIG. 7. Comparison between the script calculation for the SRS propagation and the inline one. The green curves are the non-SRS results for IB absorption, the black curves include SRS depletion and the red curves show the SRS intensity.

ACKNOWLEDGMENTS

We gratefully acknowledge useful discussions with Gary Kerbel, Pierre Michel and David Strozzi. This work was performed under the auspices of the U.S. Department of Energy by Lawrence Livermore National Laboratory under Contract DE-AC52-07NA27344.

[1] W. L. Kruer, S. C. Wilks, B. B. Afeyan, and R. K. Kirkwood, Phys. Plasmas **3**, 382 (1996).

[2] V. V. Eliseev, W. Rozmus, V. T. Tikhonchuk, and C. E. Capjack, Phys. Plasmas **6**, 3 (1996).

[3] P. Michel, L. Divol, E. A. Williams, S. Weber, C. A. Thomas, D. A. Callahan, S. W. Haan, J. D. Salmonson, S. Dixit, D. E. Hinkel, M. J. Edwards, B. J. MacGowan, J. D. Lindl, S. H. Glenzer, and L. J. Suter, Phys. Rev. Lett. **102**, 025004 (2009).

[4] P. Michel, L. Divol, E. A. Williams, C. A. Thomas, D. A. Callahan, S. Weber, S. W. Haan, J. D. Salmonson, N. B. Meezan, O. L. Landen, S. Dixit, D. E. Hinkel, M. J. Edwards, B. J. MacGowan, J. D. Lindl, S. H. Glenzer, and L. J. Suter, Phys. Plasmas **16**, 042702 (2009).

[5] P. Michel, S. H. Glenzer, L. Divol, D. K. Bradley, D. Callahan, S. Dixit, S. Glenn, D. Hinkel, R. K. Kirkwood, J. L. Kline, W. L. Kruer, G. A. Kyrala, S. L. Pape, N. B. Meezan, R. Town, K. Widmann, E. A. Williams, B. J. MacGowan, J. Lindl, and L. J. Suter, Phys. Plasmas **17**, 056305 (2010).

[6] S. H. Glenzer, B. J. MacGowan, P. Michel, N. B. Meezan, L. J. Suter, S. N. Dixit, J. L. Kline, G. A. Kyrala, D. K. Bradley, D. A. Callahan, E. L. Dewald, L. Divol, E. Dzenitis, M. J. Edwards, A. V. Hamza, C. A. Haynam, D. E. Hinkel, D. H. Kalantar, J. D. Kilkenny, O. L. Landen, J. D. Lindl, S. LePape, J. D. Moody, A. Nikroo, T. Parham, M. B. Schneider, R. P. J. Town, P. Wegner, K. Widmann, P. Whitman, B. K. F. Young, B. Van Wonterghem, L. J. Atherton, and E. I. Moses, Science **327**, 1228 (2010).

[7] G. A. Kyrala, J. L. Kline, S. Dixit, S. Glenzer, D. Kalantar, D. Bradley, N. Izumi, N. Meezan, O. Landen, D. Callahan, S. V. Weber, J. P. Holder, S. Glenn, M. J. Edwards, J. Koch, L. J. Suter, S. W. Haan, R. P. J. Town, P. Michel, O. Jones, S. Langer, J. D. Moody, E. L. Dewald, T. Ma, J. Ralph, A. Hamza, E. Dzenitis, and J. Kilkenny, Physics of Plasmas **18**, 056307 (2011).

[8] P. Michel, L. Divol, R. P. J. Town, M. D. Rosen, D. A. Callahan, N. B. Meezan, M. B. Schneider, G. A. Kyrala, J. D. Moody, E. L. Dewald, K. Widmann, E. Bond, J. L. Kline, C. A. Thomas, S. Dixit, E. A. Williams, D. E. Hinkel, R. L. Berger, O. L. Landen, M. J. Edwards, B. J. MacGowan, J. D. Lindl, C. Haynam, L. J. Suter, S. H. Glenzer, and E. Moses, Phys. Rev. E **83**, 046409 (2011).

[9] J. D. Moody, P. Michel, L. Divol, R. L. Berger, E. Bond, D. K. Bradley, D. A. Callahan, E. L.

Dewald, S. Dixit, M. J. Edwards, S. Glenn, A. Hamza, C. Haynam, D. E. Hinkel, N. Izumi, O. Jones, J. D. Kilkenn, R. K. Kirkwood, J. L. Kline, W. L. Kruer, G. A. Kyrala, O. L. Landen, S. LePape, J. D. Lindl, B. J. MacGowan, N. B. Meezan, A. Nikroo, M. D. Rosen, M. B. Schneider, D. J. Strozzi, L. J. Suter, C. A. Thomas, R. P. J. Town, K. Widmann, E. A. Williams, L. J. Atherton, S. H. Glenzer, and E. I. Moses, Nature Phys. **8**, 344 (2012).

[10] D. Edgell, W. Seka, J. Delettrez, R. Craxton, V. Goncharov, I. Igumenshchev, J. Myatt, A. Maximov, R. Short, T. Sangster, and R. Bahr, Bull. Am. Phys. Soc. **54**, 145 (2009).

[11] I. V. Igumenshchev, W. Seka, D. H. Edgell, D. T. Michel, D. H. Froula, V. N. Goncharov, R. S. Craxton, L. Divol, R. Epstein, R. Follett, J. H. Kelly, T. Z. Kosc, A. V. Maximov, R. L. McCrory, D. D. Meyerhofer, P. Michel, J. F. Myatt, T. C. Sangster, A. Shvydky, S. Skupsky, and C. Stoeckl, Physics of Plasmas **19**, 056314 (2012).

[12] D. H. Froula, I. V. Igumenshchev, D. T. Michel, D. H. Edgell, R. Follett, V. Y. Glebov, V. N. Goncharov, J. Kwiatkowski, F. J. Marshall, P. B. Radha, W. Seka, C. Sorce, S. Stagnitto, C. Stoeckl, and T. C. Sangster, Phys. Rev. Lett. **108**, 125003 (2012).

[13] The frequency shifts are averaged over the finite bandwidths of the lasers due to smoothing by spectral dispersion, i.e. 45 GHz on NIF and 1 THz at Omega.

[14] E. A. Williams, D. E. Hinkel, and J. A. Hittinger, in *Inertial Fusion Sciences and Applications 2003* (The American Nuclear Society, 2004) p. 252.

[15] E. A. Williams, B. I. Cohen, L. Divol, M. R. Dorr, J. A. Hittinger, D. E. Hinkel, A. B. Langdon, R. K. Kirkwood, D. H. Froula, and S. H. Glenzer, Phys. Plasmas **11**, 231 (2004).

[16] R. P. J. Town, M. D. Rosen, P. A. Michel, L. Divol, J. D. Moody, G. A. Kyrala, M. B. Schneider, J. L. Kline, C. A. Thomas, J. L. Milovich, D. A. Callahan, N. B. Meezan, D. E. Hinkel, E. A. Williams, R. L. Berger, M. J. Edwards, L. J. Suter, S. W. Haan, J. D. Lindl, E. L. Dewald, S. Dixit, S. H. Glenzer, O. L. Landen, E. I. Moses, H. A. Scott, J. A. Harte, and G. B. Zimmerman, Physics of Plasmas **18**, 056302 (2011).

[17] P. Michel, W. Rozmus, E. A. Williams, L. Divol, R. L. Berger, S. H. Glenzer, and D. A. Callahan, Physics of Plasmas **20**, 056308 (2013).

[18] This expression applies to randomly polarized laser beams or to NIF quads with mixed polarizations; for the case of two laser beams with linear polarizations, one needs to replace the $(1+\cos^2\theta_{\alpha\beta})$ term by $4\cos\theta_\epsilon$, where θ_ϵ is the angle between the polarization vectors of the two fields.

[19] A. Friedman, *3D Laser Transport Algorithm*, External Report UCRL-93644 (Lawrence Livermore National Laboratory, 1985).

[20] Note that $\alpha_{1,2} = 16\,\pi r_e/m_e c^2/(k^v_{1,2}\,\omega_{1,2})$; for a $1.06\,\mu m$ laser, the natural SI intensity is $1.1766 \cdot 10^{18}\,W/cm^2$.

[21] P. Michel, W. Rozmus, E. A. Williams, L. Divol, R. L. Berger, R. P. J. Town, S. H. Glenzer, and D. A. Callahan, Phys. Rev. Lett. **109**, 195004 (2012).

[22] J. A. Harte and G. B. Zimmerman, *Lasnex Pondermotive Force Algorithm*, Internal Report UCID-17517 (Lawrence Livermore National Laboratory, 1977).

[23] The Lasnex simulation is by R.P.J. Town, and is a "post-shot" from the NIF symcap shot N110807 near the time of maximum peak laser power, t=19.5 ns. It is the "first iteration" of the two successive Lasnex runs typically done to calculate a post-shot, i.e. it is run with the "as-shot" laser power: the backscatter is not removed, and the CBET multipliers are not applied.